EES Catalysis

PAPER

View Article Online
View Journal | View Issue

Cite this: *EES Catal.*, 2025, 3, 743

Leveraging oxygen mobility with zirconia in low-temperature plasma for enhanced methane reforming to syngas†

FNU Gorky,[a] Levi Pile,[a] Grace Jones,[a] Apolo Nambo,[b] Mourad Benamara[c] and Maria L. Carreon *[a]

Despite extensive efforts to optimize the single-step production of syngas, hydrocarbons, and oxygenates *via* plasma catalysis, several challenges remain unresolved. In particular, understanding the various reaction pathways is hindered by the complexity of the reactions and the diverse range of chemical products formed. In this study, our main objective is to evaluate and compare the influence of zirconia on reaction pathways, methane (CH_4) and carbon dioxide (CO_2) conversions (%), and syngas selectivity (%) relative to the plasma-only route. Experiments were conducted at a low radio-frequency plasma power of 50 Watts without external heating. The results demonstrated significantly enhanced conversions of carbon dioxide and methane when the reaction chamber was packed with zirconia (ZrO_2). Methane conversion was observed to be the highest at a rich CO_2 feed [$CO_2 : CH_4$ (2 : 1)], while plasma only revealed conversion of 20.1%. After packing with zirconia, the conversion increased to 71.2% (3.5 times increment). On the other hand, carbon dioxide conversions were also observed to be the highest at a feed composition of $CO_2 : CH_4$ (2 : 1), with plasma only (13.6%) *vs.* with zirconia packing (60.9%) revealing a 4.4 times increase. Interestingly, at the rich CO_2 feed composition, the syngas product (CO + H_2) selectivity increased after packing ZrO_2 by 1.1 times for CO and 1.2 times for H_2. Optical emission spectroscopy (OES) analysis revealed important insights into the gas phase, with signatures of atomic oxygen (O) being the dominant plasma species in the gas phase under plasma-only conditions, while their intensities plummeted when zirconia was introduced, indicating active oxygen diffusion onto the surface of zirconia. Raman spectroscopy and X-ray photoelectron spectroscopy (XPS) confirmed important surface alterations after plasma exposure and most importantly provided experimental proof on zirconia's oxygen mobility. These findings provided an integral perspective into the design of catalytic materials that enhance oxygen mobility, enabling low-temperature and energy-efficient dry methane reforming for a sustainable future.

Received 10th March 2025,
Accepted 5th May 2025

DOI: 10.1039/d5ey00069f

rsc.li/eescatalysis

Broader context

Global energy demands and the urgent need to combat climate change call for innovative approaches that convert raw materials into cleaner fuels. In this context, dry methane reforming (DRM) emerges as a promising route to valorize methane and carbon dioxide, transforming greenhouse gases into syngas. Our research aims to understand the oxygen mobility of zirconia within a low-temperature, electron-mediated plasma environment to unravel mechanistic insights that address two challenges: enhancing syngas yields at room temperature and mitigating catalyst deactivation from carbon deposition. Comprehensive gas phase and surface analysis revealed zirconia's ability to shuttle oxygen between its lattice and surface sustains dynamic redox cycles, encouraging plasma driven activation pathways for methane and CO_2 and simultaneously gasifying nascent carbon deposits to prevent coking. Compared with the conventional route DRM, our plasma catalytic system achieves significant reductions in energy input, and prolonged catalyst stability. These findings inform the rational design of oxygen mobility focused materials, paving the way for scalable, decentralized syngas production and next-gen electrified energy conversion technologies.

[a] *Ralph E. Martin Department of Chemical Engineering, University of Arkansas, 3202 Bell Engineering Center, Fayetteville, Arkansas 72701-1201, USA. E-mail: mc138@uark.edu*
[b] *Bert Thin Films, LLC., 625 Myrtle St, Louisville, KY 40298, USA*
[c] *Materials Science and Engineering Program, Institute for Nanoscience and Engineering, University of Arkansas, Fayetteville, AR, 72701, USA*

† Electronic supplementary information (ESI) available. See DOI: https://doi.org/10.1039/d5ey00069f

1. Introduction

The dry reforming of methane (DRM) is a chemical reaction in which methane (CH_4) and carbon dioxide (CO_2) react to form synthetic gas (syngas), a mixture of hydrogen (H_2) and carbon monoxide (CO). DRM is a well-studied and highly endothermic

reaction (see eqn (1)) and requires high temperatures (800–1000 °C) and moderate (1–10 bar) to high (20–30 bar) pressures.[1]

$$CH_4 + CO_2 \rightarrow 2CO + 2H_2, \quad \Delta H^\circ = +247 \text{ kJ mol}^{-1} \qquad (1)$$

The interest in DRM has grown to utilize CO_2 to obtain value-added products and to make use of high CO_2 content natural gas deposits that cannot be economically used for steam reforming.[1,2]

Traditionally, hydrocarbons and oxygenate production has relied on multi-step thermal catalytic processes involving decomposition of CH_4 and CO_2 at elevated temperatures (800–1000 °C) and pressures (20–50 bar) towards the production of synthetic gas. To further produce essential chemicals, the produced syngas is further processed through another step *via* the Fischer–Tropsch synthesis (temperatures of 250–350 °C and pressures of 20–50 bar) to produce hydrocarbons and oxygenates, such as alkanes, aldehydes, ketones, and alcohols. While effective, these steps are energy-intensive and economically demanding, driving researchers to explore alternative catalytic routes that reduce energy consumption. The growing urgency to mitigate greenhouse gas emissions while producing value-added chemicals has increased the interest in various catalytic routes such as plasma-catalytic DRM.[3,4]

The activation of methane and carbon dioxide poses a significant challenge in thermal catalytic processes due to their high bond dissociation energies of 434.2 kJ mol^{-1} for C–H in CH_4 and 530.7 kJ mol^{-1} for C═O in CO_2. These conditions necessitate extreme temperatures, which often lead to the decomposition of intermediates, limiting single pass conversions and selectivity. The search for energy alternatives positions non-thermal plasma (NTP) as a promising alternative, enabling efficient activation of CH_4 and CO_2 under mild conditions (room temperature and atmospheric pressure). By generating high-energy electrons in a low-temperature environment, NTP offers a non-selective but energy-efficient alternative to produce syngas,[5–7] hydrocarbons[8–10] and oxygenates[11–13] in a single step.

Specifically for the partial oxidation of methane (POM), studies have shown that oxygen can effectively activate methane in plasma environments; however, excessive oxidation frequently results in the overproduction of CO_2 and undesired byproducts.[14] Using CO_2 as a milder oxidant offers dual benefits: mitigating two of the most prevalent greenhouse gases while producing valuable chemicals. For the specific case of plasma-catalysts the resulting synergy enables partial oxidation pathways that favor the formation of oxygenates and hydrocarbons as products, presenting an alternative under mild conditions for the DRM.[15–17]

Catalyst design and plasma-catalyst synergy is critical to advancing plasma-catalytic processes. While precious metals have traditionally dominated catalytic applications due to their superior performance, their high cost and limited availability make them economically unfeasible for large-scale implementation.[18] Research has increasingly focused on earth-abundant materials, such as silica, alumina, and zirconia, which offer comparable catalytic performance under specific conditions. However, findings from thermal catalysis do not always translate seamlessly into plasma catalysis, needing a deeper understanding of material behavior under plasma conditions.

In thermal catalytic research, high temperatures (800–850 °C) are required for achieving higher efficiencies of CH_4 and CO_2 conversions. Supports like silica,[19] alumina,[20] and zirconia[21] are commonly used impregnated with transition metals as catalysts. Zirconia is highly stable over high temperatures making it suitable for sustaining multiple cycles.[22] Literature reports, at the relatively low temperature of 600 °C, show that Ni–Zr on MCM-41 achieved 91% methane conversion,[23] highlighting the effectiveness of zirconia-based supports even under moderate conditions. Similarly, Pt-impregnated ZrO_2 at 700 °C exhibited 80.1% methane and 84.6% CO_2 conversion,[24] surpassing Ni-based catalysts at the same temperature. The introduction of Ni with a Zr promoter at 700 °C improved the conversion to 73% for methane and 76.7% for CO_2,[25] displaying the role of metal promoters in enhancing catalytic activity. Overall, zirconia-based catalysts with Pt and Ni–Zr combinations demonstrated higher conversion at lower temperatures with less metal loading, making them more efficient for high-temperature thermal catalysis.

In plasma-catalytic systems, zirconia-based materials displayed promising performances. In particular, zirconia and ceria based oxides like Ni–$Ce_xZr_{1-x}O_2$ within a dielectric barrier discharge (DBD) plasma reactor enable CO_2 conversions up to 80% with 100% methane selectivity at temperatures as low as 90 °C, whereas in thermal catalysis temperatures above 300 °C were required to achieve comparable results.[26] Plasma activation of CO_2 resulted in the formation of CO* and O* species, facilitating enhanced conversion rates at lower temperatures.[27–29] Furthermore, hydrogen plasma treatment of Ni-based ceria-zirconia catalysts was found to be an effective alternative to conventional thermal reduction, maintaining similar catalytic activity and strengthening Ni-support interactions.[30] The role of Ce and Zr promoters in hydrotalcite-derived catalysts was also examined, displaying that while Zr-containing catalysts exhibited higher activity under plasma conditions, the overall impact of these promoters on catalytic performance remained minimal.[31] In plasma catalysis literature, zirconia based materials have been employed for CO_2 hydrogenation, however, while designing the materials, the impregnation of multiple metals and ceramics makes it challenging to isolate the individual contributions. In this study, we employed pristine zirconia to investigate the effect of oxygen mobility and its effect towards product distribution during dry methane reforming. Zirconia stands out as an ideal candidate for plasma-catalytic DMR due to its intrinsic oxygen mobility, structural stability under harsh conditions, and potential to mitigate coke formation. Coking, a persistent challenge in methane reforming, significantly degrades catalyst performance by blocking the active surface with carbon build-up.[21] The oxygen mobility in zirconia's matrix facilitates the active removal of amorphous carbon species, preventing their buildup and prolonging catalyst life. Furthermore, the porous structure of zirconia offers the possibility to enhance its interaction with plasma, improving methane decomposition towards value added products.

Our group has previously explored NTP (RF and DBD) applications for various chemistries including ammonia synthesis,[32–38] dry methane reforming,[13] plastics decomposition to fuels,[39,40] methane upgrading,[8] graphene synthesis from biomass,[41] greenhouse gas plasma based membrane separation,[42] carbon capture and plasma based desorption,[43] using various catalysts such as inorganic metal oxides,[35,38,44,45] low-metaling point alloys,[46,47] perovskites,[34,39] zeolites,[8,32,43,48] hybrid materials such as MOFs,[13,36,49] and porous organic materials such as CC3[50] for storage and catalytic applications showing the importance of tailoring materials for plasma.

Although the industry typically produces syngas *via* coal gasification[51] and steam reforming of methane,[52] dry methane reforming (DMR) has attracted significant research interest over the past several decades because it incorporates carbon dioxide, a major pollutant, into useful products; however, the DRM reaction has faced major challenges, such as catalyst deactivation due to coking at high temperatures. Building on the extensive literature covering both thermal and plasma catalytic DRM, our study involves lowering the amount of energy required to activate reactants, with the objective of enhancing syngas production, while employing commercial materials like zirconia. Building on extensive studies of both thermal and plasma-catalytic dry reforming of methane, we aimed to minimize the energy needed to activate CH_4 and CO_2 under low-temperature plasma. To achieve this, we selected commercial zirconia for its exceptional suitability to plasma environments because it combines outstanding thermal stability, chemical inertness to corrosive species, resistance to sintering and phase changes, and high mechanical hardness, which all help it sustaining the energetic particle collisions during plasma discharges. Materials like zirconia, known for its oxygen vacancy, provide a reactive surface that can interact with plasma activated species (CO_2*, O*) in a manner conceptually similar to that described in the recent plasma catalytic chemical looping system[53] involving $Ce_{0.7}Zr_{0.3}O_2$.[54] In addition, zirconia's abundant oxygen vacancies facilitate rapid ion mobility, enabling it to capture and gasify nascent carbon deposits and thus suppress coking. Through this work, we are exploring key reaction pathways in plasma catalytic DRM and demonstrating an energy efficient approach. The overarching goal of our findings is to lay the groundwork for the future development of tailored zirconia-based thin films or membranes, offering a scalable, economically viable route, for converting greenhouse gases into valuable chemicals for sustainable energy conversion.

2. Experimental

2.1. Materials and methods

Commercial zirconia was provided from Luxfer MEL Technologies (Manchester, England), reference number (XZO1501/09). Fumed silica was purchased from Fasco (CAB-O-SIL® M-5).

2.2. Zirconia characterization

The commercial zirconia catalysts used in this study were degassed under vacuum at 100 °C for 5 hours. Nitrogen physisorption isotherms were measured at 77 K using a 3Flex Micrometrics instrument to determine the Brunauer–Emmett–Teller (BET) surface area, pore size, pore volume, and particle size (μm) of both fresh and plasma-exposed catalysts. The morphology of the commercial zirconia was examined using an FEI Nova Nanolab 200 Dual-Beam system, which is equipped with a high-resolution field-emission gun analytical scanning electron microscope (SEM) operating at 15 kV. The commercial zirconia was analysed using powder X-ray diffraction (XRD) with a Panalytical X'Pert Materials Research Diffractometer, employing Cu Kα radiation (λ = 1.54 Å) over a 2θ range of 20°–80°. To ensure accurate crystallinity assessment, the intensity scale (a.u.) was standardized across all catalysts. X-ray photoelectron spectroscopy (XPS) was carried out on a VersaProbe II system featuring a monochromatic Al Kα source. All XPS measurements were acquired with the electron take-off angle set at 47°. Raman spectra were recorded on a Horiba LabRAM HR micro-Raman spectrometer (Horiba Scientific) equipped with a monochromated 532 nm laser.

2.3. DMR plasma setup

The experiments were conducted in an in-house built RF plasma reactor using CO_2 (Airgas, 99.99%) and CH_4 (UHP Airgas) as reactants. The flow rates varied between 10 and 100 sccm, controlled *via* a mass flow controller (MFC). Plasma generation was achieved using an RF power supply with a Seren IPS, Inc. Matching Network. The reaction conditions included a plasma power range of 50–300 W and a pressure of 0.3 Torr, consistent across all experiments. Vacuum was maintained using an Edwards Dry scroll pump (nXDS6i). Each reaction used 1.2 g of zirconia, ensuring uniform catalyst loading across the electrode area. The vacuum pump's outlet was connected *via* copper tubing to the inlet valve of a gas chromatography (Agilent 8860) system equipped with an Agilent HP-PLOT U column 30 m × 0.320 mm × 10 μm, (see Fig. S1 for a complete schematic, ESI†). All experiments were performed in triplicates. Key plasma species were analysed using optical emission spectroscopy (OES). Light emitted from the plasma discharge was directed through an optical system, and the emission spectra of the glow region were recorded. A dual-channel ultraviolet-visible-near-infrared (UV-vis-NIR) spectrophotometer (Avantes Inc., USB2000 Series) was used in scope mode, covering a spectral range of 200–1100 nm with a 600 lines per mm grating and a resolution of 0.4 nm. A bifurcated 400-μm fiber optic cable was employed for spectral collection. Based on optimal spectroscopy conditions, the integration time was set to 5 s with 100 averages, following the methodology established in previous studies.[39]

2.4. Zirconia textural properties

Our primary investigation was dedicated towards analysing the difference in textural properties of zirconia at different calcination temperatures before conducting plasma-based reactions. The XRD revealed the effect of calcination temperature on the phases of zirconia. At 400 °C, the sample predominantly exhibits cubic phases, specifically the (111) reflection. As the temperature increases to 500 °C, both cubic (111) and monoclinic ($\bar{1}$11) phases become comparable in intensity, indicating

a phase transition. At 600 °C, the monoclinic phase ($\bar{1}11$) becomes dominant and Fig. 1a confirms the evidence of the monoclinic phase.

We conducted the calcination at 1000 °C, and the sample exclusively shows monoclinic phases ($\bar{1}11$), with no cubic phase contribution (see Fig. S2, ESI†). This temperature-dependent phase evolution highlighted the critical role of calcination temperature in selecting the desired zirconia phase, with cubic phases being the target for further study due its symmetric configuration. Cubic phases offer high surface areas as evident *via* physio-chemical properties described in the experimental table (see Table 1). Apart from surface area, it is well reported in the literature for materials like zirconia and ceria that the cubic phases offer enhanced anionic mobility[55] and redox properties,[56] and the cubic phase also offers lower elastic modulus and higher malleability over other phases such as monoclinic and tetragonal phases.[57] Based on the literature, the vacancies (defects) can be co-related with lattice relaxation observed in doped cubic zirconia. This directly implies that lower elastic modulus causes a higher degree of relaxation allowing lower binding energies with oxygen vacancy and improved mobility.[58]

The zirconia samples calcined at different temperatures revealed significant changes in surface area and structural properties. At 400 °C, ZrO_2 exhibits the highest BET surface area of 122.45 $m^2\ g^{-1}$ and pore volume of 0.49 $cm^3\ g^{-1}$, along with the smallest particle size (48.99 nm), correlating with a cubic XRD phase. As the calcination temperature increases to 500 °C, the BET surface area and pore volume decrease, while pore size and particle size grow, indicating a transition to a hybrid phase exhibiting cubic + monoclinic phases. At 600 °C, the material exhibits the lowest surface area (49.79 $m^2\ g^{-1}$) and the largest particle size (120.48 nm), dominated by the monoclinic phase (see Fig. 1b and Table 1).

Similarly, our experimental data revealed unimodal pore size distribution. At a lower calcination temperature (400 °C), the pore size was smaller (6.3 nm), whereas higher temperatures led to an increase in pore width (up to 28 nm) (see Fig. S3, ESI†). The N_2-isotherm revealed characteristics of type II isotherms, which were characterized by an initial monolayer adsorption at lower relative pressures, followed by a sharp rise that indicated multilayer adsorption at intermediate pressures. The presence of a hysteresis loop suggests the existence of pores, indicating that capillary condensation had occurred within the pores. This was classified as an IUPAC type H3 loop,[59] where the adsorption branch resembled a type II isotherm, and the lower limit of the desorption branch was typically located at the cavitation-induced p/p_0. Hysteresis loops of type H3 were associated with non-rigid aggregates of plate-like particles but also appeared when the pore network consisted of macropores that were not entirely filled with pore condensate.[59] These results revealed the influence of calcination temperature on zirconia's phase, porosity, and surface characteristics, with lower temperatures favouring the desirable cubic phase. In the literature it is well noted that cubic zirconia facilitates redox reactions, which can further enhance oxygen mobility.[60]

Table 1 Textural properties for zirconia at different calcination temperatures

Sample	ZrO_2-400	ZrO_2-500	ZrO_2-600
BET surface area ($m^2\ g^{-1}$)	122.45	76.23	49.79
Langmuir surface area ($m^2\ g^{-1}$)	163.96	104.19	67.51
Pore volume ($cm^3\ g^{-1}$)	0.49	0.46	0.39
Pore size (nm)	14.19	22.39	29.92
Particle size (nm)	48.99	78.70	120.48
t-Plot external surface area ($m^2\ g^{-1}$)	133.82	76.60	51.30

3. Results and discussion

3.1. Plasma only

Our initial investigations entailed acquiring the methane and carbon dioxide conversion with and without external cooling.

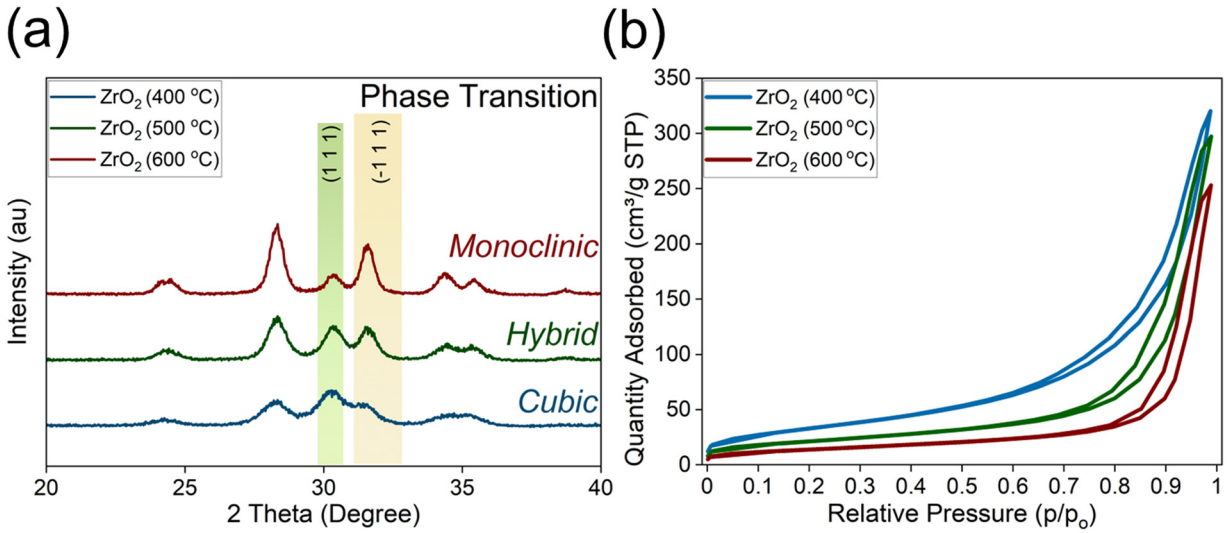

Fig. 1 (a) XRD revealing the effect of calcination temperature on ZrO_2 phases; (b) Nitrogen isotherms at different temperatures on different zirconia calcination temperatures.

A steady state for DRM reactions was observed after 45 minutes, and with long operation time, the temperature around the electrode area increased. To differentiate the effect of heat *vs.* plasma, we studied how varying plasma power will affect methane and carbon dioxide conversion. This was investigated under plasma-only conditions using an *in-house* RF (radiofrequency) plasma reactor under varying power conditions, with and without external cooling. A cooling fan was positioned near the electrode area to control temperature. The total flow rate was maintained at 25 sccm with a $CO_2:CH_4$ feed ratio of 1 : 1, and no external heating applied. All results were averaged from triplicate measurements over a reaction time of 2 hours. We selected these parameters as baseline, as most of the experimental results demonstrated that increasing plasma power led to higher methane and carbon dioxide conversion in both configurations. Without the cooling fan, methane conversion increased from 15.51% at 50 W to 42.77% at 300 W, while carbon dioxide conversion rose from 11.24% to 35.3%. A similar trend was observed with the cooling fan, where methane conversion improved from 14.83% at 50 W to 46% at 300 W, and carbon dioxide conversion increased from 10.77% to 37.53%. At all power levels, slightly higher conversions were recorded with the fan, suggesting improved reaction efficiency due to better temperature regulation near the electrodes. Additionally, standard deviations were generally lower with the external cooling, revealing more stable reaction conditions. The results highlight the significant role of plasma power in enhancing conversion efficiency and suggest that thermal management strategies, such as electrode cooling, can further optimize performance in plasma-assisted dry methane reforming. However, the comparative difference was minor and for the further studies we conducted experiments without a fan to reduce energy requirements. We also selected 50 Watts (minimal plasma power) to further explore various parameters, such as plasma power (Watts) and feed ratio ($CO_2:CH_4$), and various flow rates (sccm) to further analyze the methane and carbon dioxide conversion in a more comprehensive way (see Fig. S4, ESI†).

The effect of total flow rate on methane and carbon dioxide conversion was investigated at the minimal plasma power of 50 W to reduce energy cost. The $CO_2:CH_4$ feed ratio was maintained at 1 : 1, and no external heating was applied over a reaction time of 2 hours. The results indicated a decreasing trend in both methane and carbon dioxide conversion as the total flow rate increased. At 10 sccm, the highest methane and carbon dioxide conversions were observed at 25% and 17.20%, respectively. As the flow rate increased to 25 sccm, the conversions slightly dropped to 19.23% for methane and 15.60% for CO_2. Further increasing the flow rate to 40 sccm, 75 sccm, and 100 sccm led to a continued decline in conversions, with the lowest values recorded at 100 sccm (8.77% methane and 7.73% CO_2 conversion). The experimental observations revealed that lower flow rates favored higher reactant residence time, possibly increasing the lifetime of active species allowing for more effective plasma-activated reactions on the gas phase. On the other hand, at higher flow rates the lower residence time led to limited reactant activation and increased the possibility to undergo recombination of initial plasma species in the afterglow region, eventually leading to lower conversion efficiencies. The standard deviation values remained relatively small across all conditions, indicating consistent experimental reproducibility.

Finally, the effect of $CO_2:CH_4$ feed ratio on methane and carbon dioxide conversion was examined in the RF plasma reactor at 50 W with a total flow rate of 25 sccm. The results demonstrated that higher methane content in the feed mixture led to increased CH_4 and CO_2 conversions. The 3 : 1 ratio exhibited the highest conversions, with 26.1% for methane and 17.8% for CO_2, while a progressive decrease was observed as the CH_4 ratio increased, reaching the lowest values at 1 : 3 $CO_2:CH_4$ (9.3% methane and 7.8% CO_2 conversion). This trend suggested that excess CO_2 enhances plasma reactivity, as evident from the experimental data that higher methane rich composition can lead to methane recombination which eventually leads to lower conversion of methane (Fig. 2).

3.2. Zirconia plasma catalysis

Our next investigations lead towards understanding the impact of packed bed reaction in plasma-DRM. The packed bed containing 1.2 grams of cubic zirconia (ZrO_2) *versus* plasma-only conditions on methane and carbon dioxide conversion was evaluated in an RF plasma reactor at 50 W, with a total flow rate of 25 sccm and equimolar feed ratio. The results revealed that conversion efficiencies were widely enhanced with ZrO_2 across all feed ratios. Under plasma-only conditions, the equimolar feed (1 : 1) yielded a methane conversion of 15.5% and a CO_2 conversion of 11.97%. However, with the addition of ZrO_2 the equimolar system achieved a methane conversion of 63.73% and a CO_2 conversion of 57.19%, approximately a 4.1-fold and 4.7-fold increase, respectively. In addition, under CO_2-rich conditions (2 : 1), methane conversion improved from 20.1% to 71.2% (a 3.5-fold increase) and CO_2 conversion from 13.6% to 60.9% (a 4.4-fold increase), while under CH_4 rich conditions (1 : 2), the values increased from 11.3% to 55.1% for methane (a 4.8-fold improvement) and from 9.8% to 41.6% for CO_2 (a 4.2-fold improvement). These findings confirmed that the addition of ZrO_2 had markedly boosted conversions (%) compared to plasma-only conditions (Fig. 3). The synergistic interaction between the plasma and zirconia likely played an integral role in enhancing these conversions. ZrO_2, known for its oxygen-mobilizing capabilities, facilitated oxygen diffusion, promoting efficient redox pathways for important plasma species. Herein, these results displayed the importance of plasma-material synergy, where active oxygen species generated in plasma can interact with the zirconia surface, further driving symmetrical molecules like methane to activate and dissociate. Similar observations were also identified in thermal catalytic routes with zirconia employed as in thermal catalytic routes it displayed very high conversions for methane and carbon dioxide (see Table S1, for the complete state of the art, ESI†).

For objectivity, we compared an inert material's (silica) performance with zirconia. At similar parameters previously reported, we compared analytically using no catalyst

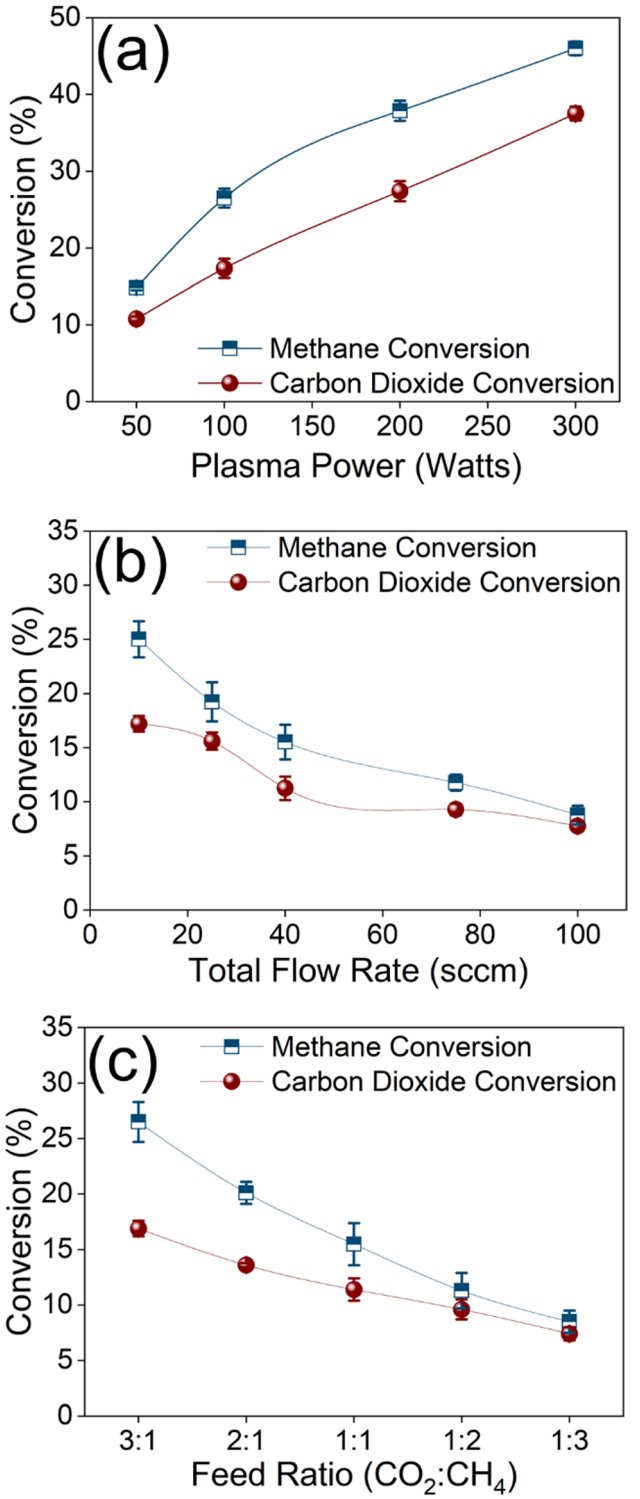

Fig. 2 Effect of methane and carbon dioxide conversion: (a) Plasma power, (b) total flow rate, and (c) feed ratio; under conditions of a plasma power of 50 Watts, no external heating, no cooling fan, and reaction time of 2 hours.

(plasma only), a packed-bed with fumed silica, and a packed-bed with zirconia, across $CO_2:CH_4$ feed ratios of 2 : 1, 1 : 1, and 1 : 2. In the plasma only setup, methane conversion decreased from 20.1% at a 2 : 1 ratio to 15.5% at 1 : 1 and 11.3% at 1 : 2, while CO_2 conversion fell from 13.6% to 12.0% and 9.9%, respectively. Introducing a silica-packed bed boosted performance: methane conversion rose to 42.8% at 2 : 1, 38.4% at 1 : 1, and 35.6% at 1 : 2, with corresponding CO_2 conversions of 29.6%, 23.4%, and 18.2%. The zirconia-packed bed delivered the highest conversions in every case, achieving 71.2% methane and 60.9% CO_2 conversions at 2 : 1, then 63.7% and 57.2% at 1 : 1, and finally 55.2% and 41.7% at 1 : 2 (see Fig. S5, ESI†). Overall, both packed-bed reactors evidently outperformed the plasma-only setup, with zirconia proving to be the most effective material for methane and carbon dioxide conversions.

This enhanced conversion directly influenced product selectivity, favouring syngas (CO and H_2) and C_2 alkane and olefins, while suppressing the formation of heavier alkanes and oxygenates. The syngas production varied with changes in the feed ratio ($CO_2:CH_4$). When comparing plasma-only operation to the zirconia-packed system, a notable increase in syngas production was observed after packing with zirconia (see Fig. 4). The comparative syngas selectivity increased +14% after zirconia packing for the CO_2-rich feed ratio (2 : 1 $CO_2:CH_4$), followed by the equimolar feed (1 : 1 $CO_2:CH_4$) with +10.9% increment in selectivity, and the methane-rich feed (1 : 2 $CO_2:CH_4$) with +8.5% increment in selectivity.

Interestingly, the highest overall syngas (H_2 + CO) production in the packed bed with zirconia occurred at the CO_2-rich feed ratio (2 : 1 $CO_2:CH_4$) with 85.06% selectivity, followed by the equimolar feed (1 : 1 $CO_2:CH_4$) with 74.13% selectivity, and the methane-rich feed (1 : 2 $CO_2:CH_4$) with 60.23% selectivity. The increased interaction of the zirconia surface with oxygen species likely facilitated CO_2 activation, enhancing syngas yield. Additionally, olefin (C_2H_4) selectivity improved at a methane rich feed ratio (1 : 2 $CO_2:CH_4$) with plasma only at 14% selectivity and 11.5% with zirconia, suggesting stronger plasma recombination of methane derived active species that leads to olefins. Conversely, alkane production was observed to be the highest at a methane rich feed ratio with ethane (C_2H_6) selectivity for plasma only *vs.* zirconia (16.5% *vs.* 12.8%), while a small fraction of propane (C_3H_8) selectivity was observed to be slightly higher with plasma only *vs.* zirconia (1.5% *vs.* 1.4%). This decline suggests that the selectivity of the products was favoured towards syngas, rather than light hydrocarbons (C_2–C_3) (see Fig. 4).

In particular, in the case of the methane-rich feed composition (1 : 2 $CO_2:CH_4$) the syngas production, CO selectivity increased from 30.7% for the plasma-only to 35.9% for the zirconia-packed bed, while H_2 selectivity significantly increased from 20.8% to 24.2%. The increased availability of active oxygen species on the zirconia surface likely facilitated CO_2 activation and oxygen mobility, further improving the syngas yield. Additionally, olefin (C_2H_4) selectivity decreased from 14.4% (plasma only) to 11.5% (zirconia), displaying no enhancement on methane upgrading towards olefins over zirconia. While alkane production remained relatively higher in plasma only, observed with ethane (C_2H_6) selectivity (16.5% *vs.* 12.8%), the propane (C_3H_8) selectivity remained constant from 1.5% to 1.4% suggesting that the

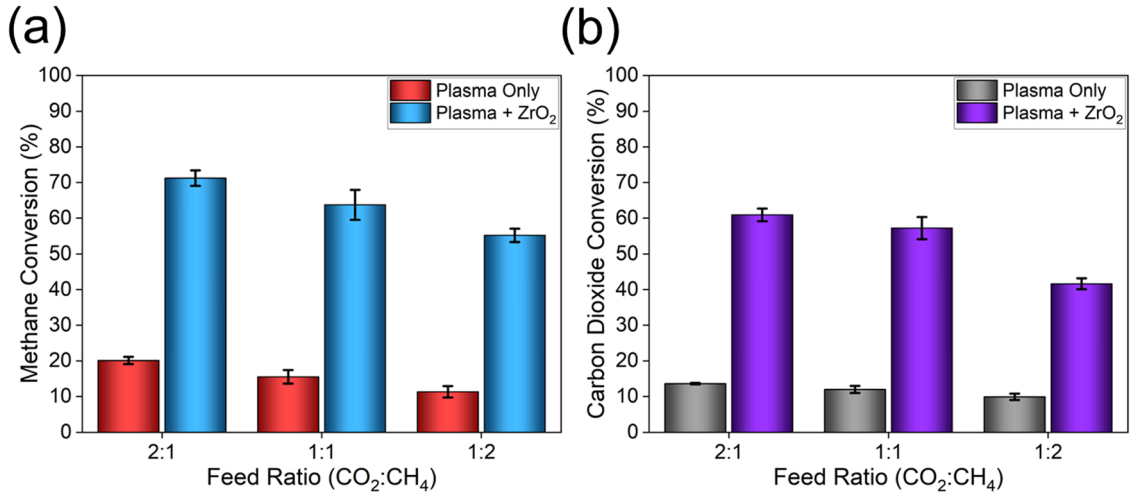

Fig. 3 Comparing (a) methane and (b) carbon dioxide conversions with plasma-only *vs.* packed bed reactor with zirconia at a total flow rate: 25 sccm, at different feed ratios ($CO_2:CH_4$), plasma power: 50 Watts, reaction time: 2 hours.

zirconia surface promoted single carbon–hydrogen species consumption into methane reforming towards syngas rather than their recombination to alkane formation (see Fig. 4a). Furthermore, oxygenated compounds such as formaldehyde selectivity slightly increased (2% *vs.* 3.7%), while acetone production decreased (0.6% to 0.2%). Interestingly, trace amounts of methanol (0.1%) and ethanol (0.05%) were detected only in the zirconia-packed system (Fig. 4b), indicating improved oxygen interaction between plasma and zirconia. The trends observed with rich methane feed improved more with an equimolar feed (Fig. 4c and d) and the best selectivity was observed with the CO_2 rich feed 2 : 1 ($CO_2:CH_4$) (Fig. 4e and f) with minor fraction of oxygenated compounds such as aldehydes, ketones and alcohols. Formaldehyde and acetone were observed to be the highest with plasma only at the CO_2 rich feed (5% and 0.9%).

Moreover, we compared the product selectivity performances with the silica packed bed, please see Fig. S6 (ESI†). For syngas, in the plasma-only mode, CO selectivity was 39.5%, rising to 41.1% over silica and to 46.5% over zirconia. Hydrogen selectivity dropped from 23.7% in plasma alone to 18.3% with silica but rose to 27.6% with zirconia. In the case of alkenes, ethylene selectivity increased from 13.1% in the bare plasma to 15.2% on silica before falling to 8.6% on zirconia, while (alkanes) ethane rose moderately from 15.4% (plasma only) to 17.2% (silica) then fell to 11.1% (zirconia). Propane selectivity was low in all configurations but increased gradually from 0.6% to 1.0% to 1.7% across plasma, silica, and zirconia.

Furthermore, to investigate zirconia's properties after plasma exposure, we conducted experiments with three cycles (6 hours) to check the stability at 50 Watts of RF plasma power. The results revealed no critical changes in crystallinity or phases observed, uncovering robustness for long DRM operations (see Fig. 5).

Similarly, no textural or morphological changes were observed for all three cycles on SEM images (see Fig. S7, ESI†), the zirconia-packed reactor exhibited only minimal declines in activity, highlighting its stability under extended operation (see Fig. S8, ESI†). At a $CO_2:CH_4$ feed ratio of 2 : 1, methane conversion decreased gently from 71.2% in the first cycle to 70.1% in the second and 68.2% in the third, while CO_2 conversion decreased from 60.9% to 58.8% and 58.1%, respectively. A similar trend was seen at a 1 : 1 feed ratio, where methane conversion dropped from 63.7% to 61.8% and then to 60.3%, and CO_2 conversion dropped from 57.2% to 55.3% and 54.8%. Under methane rich feed (1 : 2), methane conversion only edged down from 55.2% to 53.3% and 52.8%, with CO_2 conversion moving from 41.7% to 40.2% then to 39.2%. These slight decreases on the order of 2–3 percentage points over 6 hours demonstrated that zirconia maintained high reactivity and conversion (%) with minimal deactivation over extended plasma exposure.

3.3. Gas phase analysis

We conducted detailed optical emission spectroscopy (OES) analyses for both the combined CO_2 + CH_4 feed and for pure CO_2 and CH_4 feeds. Under pure CO2 conditions (Fig. S9, ESI†) the intensity of atomic oxygen species, as observed at wavelengths of 777 nm ($3s^5S^0 \rightarrow 3p^5P$) and 844 nm ($3s^3S^0 \rightarrow 3p^3P$), was significantly lower in the zirconia-packed system compared to the plasma-only configuration, 3807 a.u. and 3245a.u.(zirconia) *versus* 56 445a.u.and 59 645a.u.(plasma-only), respectively (see Fig. S9, ESI†). This reduction suggested that reactive oxygen species (ROS) were effectively mobilized from the gas phase towards the zirconia surface, consistent with heterogeneous kinetics wherein nearly all of the reaction occurs on a solid surface.[61] When looking at the interactions of pure CH4 plasma and zirconia packed bed-Plasma, we observed a small reduction in the CH* EOS signal, highlighting that carbon species derived from CH_4 plasma have little interaction with zirconia, and this small interaction was enough to increase the H signals more than 2 times. When a mixture of gasses is used, CO and H are the predominant species in the EOS analysis, increasing dramatically in the zirconia-plasma system. Based on the experimental data, it was evident that CO* (297 nm) and hydrogen-alpha (656.3 nm) surged significantly when the feed composition changed from methane rich (1 : 2) $CO_2:CH_4$ to equimolar and CO_2 rich feed ratios, and this

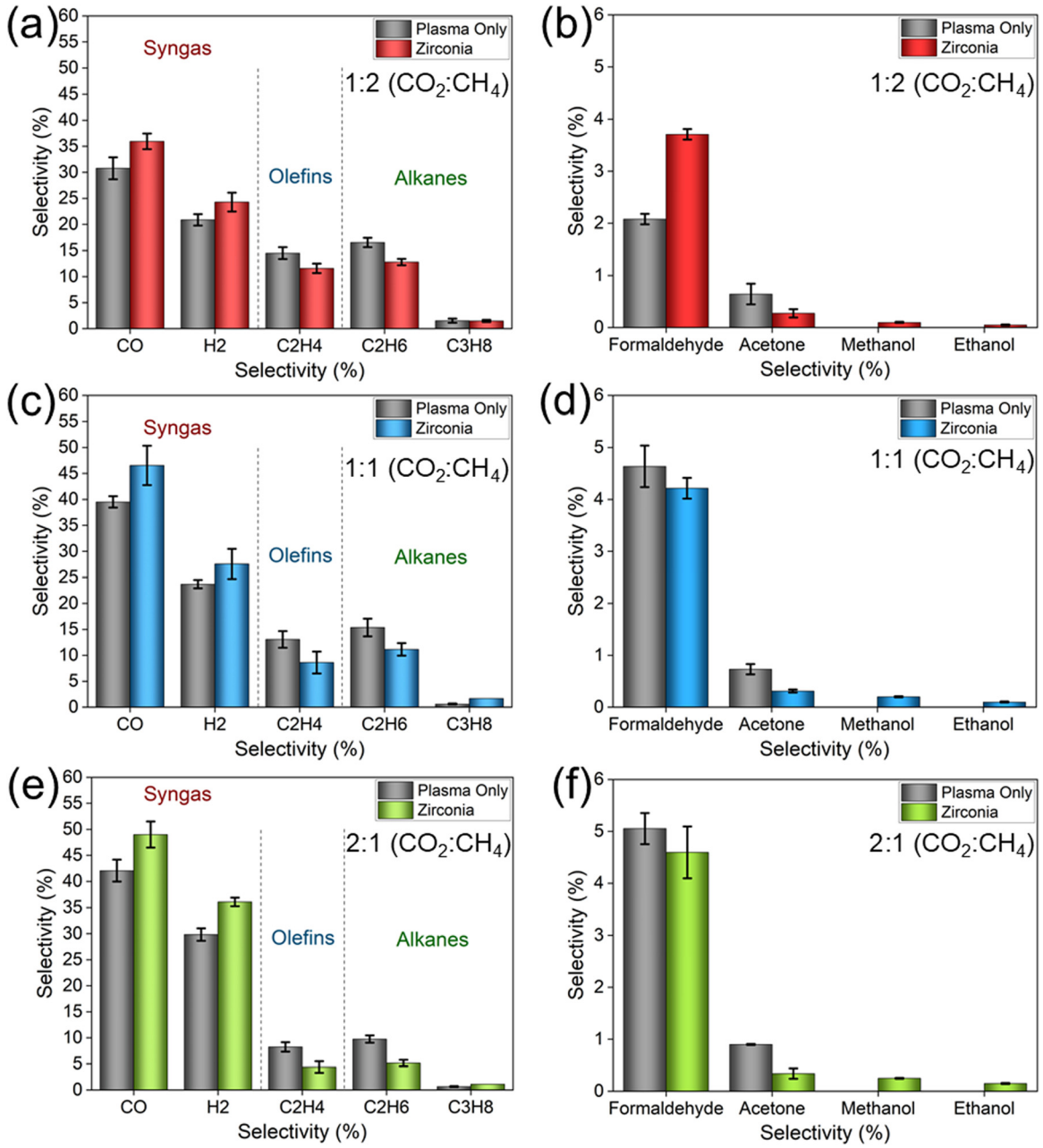

Fig. 4 Dry methane reforming product distribution. (a) Gas product distribution (syngas, olefins, alkanes), (b) oxygenate product distribution (aldehydes, ketones, alcohols) at a rich methane feed ratio (1 : 2 CO_2 : CH_4); (c) gas product distribution, (d) oxygenate product distribution at an equimolar feed ratio (1 : 1 CO_2 : CH_4); (e) gas product distribution, (f) oxygenate product distribution at a rich carbon dioxide feed ratio (2 : 1 CO_2 : CH_4); for zirconia and plasma only, at a total flow rate: 25 sccm, feed ratio: varied (CO_2 : CH_4), plasma power: 50 Watts, reaction time: 2 hours.

trend was also reported by Devid *et al.*[62] (see Fig. 6). This enhancement in reactive species correlated with a significant shift in product selectivity; for instance, the zirconia system yielded increased selectivity towards syngas further supporting the conclusion that the zirconia altered the reaction pathway by enhancing the generation of specific gas-phase intermediates.

3.4. Plausible plasma activation (gas phase)

Electrons (e^-) and excited species (*) driven bond cleavage:

CO_2 activation:

$$CO_2 + e^- \rightarrow CO^* + O^* \quad \text{(general pathway, OES displays CO* dominance)}$$

$$CO_2 \rightarrow CO_{2^+} + e^- \quad \text{(ionization)}$$

CH_4 activation:

$$CH_4 + 3e^- \rightarrow CH^* + 3H^*$$

3.5. Surface analysis

Gas phase analysis provided important insights. However, it is limited in its ability to fully characterize the material surface

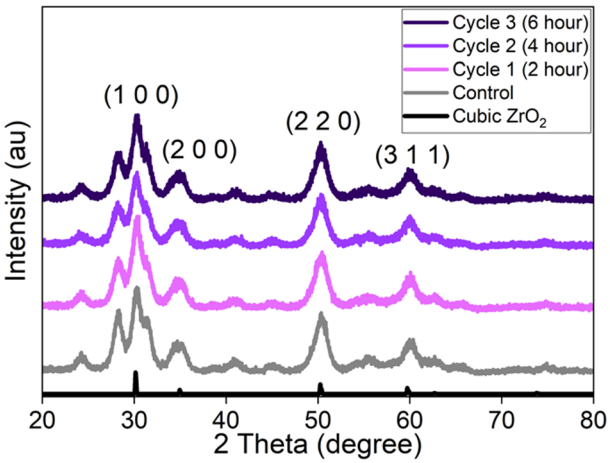

Fig. 5 XRD revealing the effect of plasma exposure with multiple cycles on ZrO_2 phases, revealing longevity and stability to cubic zirconia, at a total flow rate: 25 sccm, feed ratio: 1 : 1 (CO_2 : CH_4), plasma power: 50 Watts, reaction time: 2 hours.

(zirconia). To gain a complete understanding of the overall reaction, we performed Raman spectroscopy. After plasma treatment, the zirconia samples exhibited changes in Raman intensity. The bands at 532 cm^{-1} (Zr–O stretching)[63] and 560 cm^{-1} (oxide-vacancy vibration)[64] well defined in the control (see Fig. 7), disappeared after plasma exposure confirming the role of zirconia's oxygen mobility during the DRM reaction. Furthermore, we conducted XPS analysis, and binding energies for zirconia before and after plasma exposure are presented in Table 2. In general, the binding energy (eV) reduced for zirconia after plasma exposure, and the deconvoluted XPS analysis revealed that pure zirconia exhibited an O 1s lattice oxygen (Zr–O) peak at 529.39 eV with a 43.9% area, whereas after plasma exposure the peak shifted to 529.11 eV with a 42.2% area (see Fig. 8a and c). This minor alteration indicated a modification in the lattice oxygen associated with the formation of oxygen vacancies. The surface hydroxyl (Zr–OH) component in the control sample was observed at 530.93 eV with a 56.0% area, shifting to 530.51 eV with a 42.9% area after plasma exposure, confirming the reduction of hydroxyl groups during the reaction (see Fig. 8a and d). Interestingly, a new O 1s peak appeared at 532.65 eV with a 14.8% area after plasma exposure, explicitly representing the formation of C–O species on the surface (see Fig. 8a and c).

Zr 3d spectra represented the two split peaks which described the spin–orbit coupling, where the 3d electrons split into two distinct energy levels (5/2 and 3/2) for the $Zr4^+$ state. An analysis of the Zr 3d region demonstrated that the Zr $3d_{5/2}$ peak shifted from 181.59 eV with a 45.7% area in pure zirconia to 181.39 eV with a 50.1% area after plasma treatment, and the Zr $3d_{3/2}$ peak shifted from 183.92 eV with a 54.2% area to 183.74 eV with a 49.8% area which may correspond to the changes in local rearrangements in Zr^{4+} sites (see Fig. 8b and d). Reported binding energies (eV) were consistent with literature values (see Table S2 for details, ESI†).

Based on the observations it is confirmed that the RF plasma dry methane reforming slightly modified the zirconia surface. These modifications, in turn, supported increased

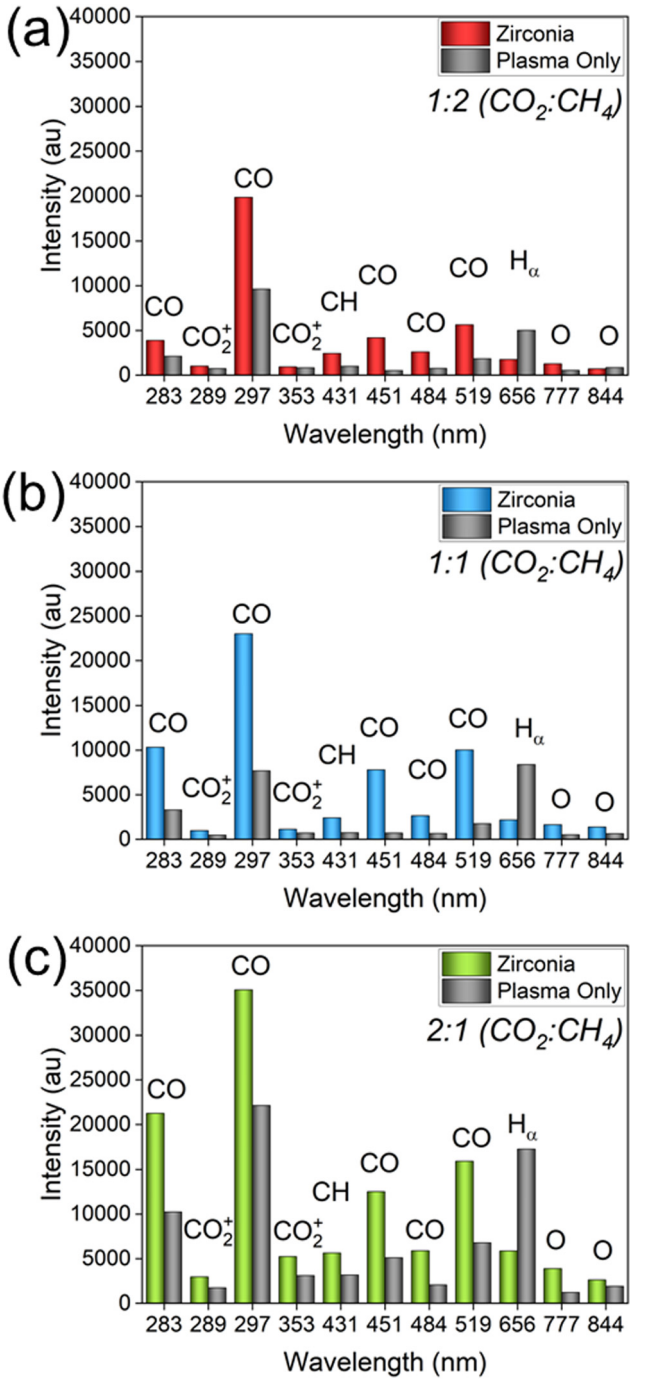

Fig. 6 Dry methane reforming plasma-catalytic gas phase; (a) methane rich feed 1 : 2 (CO_2 : CH_4); (b) equimolar feed 1 : 1 (CO_2 : CH_4); (c) carbon dioxide rich feed 2 : 1 (CO_2 : CH_4); displaying important plasma species at various feed ratios (CO_2 : CH_4), and a total flow rate of 25 sccm, plasma power: 50 Watts, reaction time: 2 Hours.

oxygen mobility and accelerated the continuous removal and conversion of surface carbon to CO during the plasma catalytic dry reforming reaction.[65–68]

3.6. State of the art and plausible mechanism

While comparing the presented results with the literature, it is important to mention in the literature various plasma sources

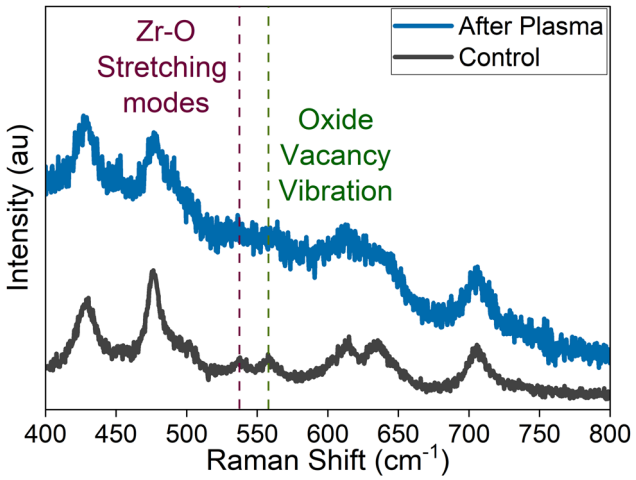

Fig. 7 Comparative Raman spectra of zirconia samples demonstrating the Zr–O stretching mode and oxide vacancy vibration features in control *vs.* sample exposed after plasma.

were evaluated for DRM over a wide range of applied powers at equimolar feed ratios from low power plasma sources DBD (7–40 Watts)[12,13,16,69,70] to high power sources of RF plasma (25–150 Watts),[62] gliding arc (GA)[71] with 165 Watts, and microwave (MW)[72,73] with 1000–3000 Watts, without catalysts and additional packing materials. In our presented work low-power radiofrequency (RF) plasma at 50 W without any catalyst achieved CH_4 and CO_2 conversions of 16.5% and 11.9%, respectively. Plasma material synergy plays an integral role in enhancing the methane and carbon dioxide conversions. Moreover, it has been demonstrated by various researchers that transition metals on alumina,[70,74] silica,[75] zeolites[70] and MOFs,[13] DMR can be selectively controlled towards the desired products. However, it is important to note that due to limited resources and growing urgency for rare earth metals, researchers are focusing on improving design and incorporating earth abundant materials.[18,76] Herein, a highly stable material such as zirconia was introduced at low power (50 W), enhancing the conversions markedly to 63.7% for CH_4 and 57.1% for CO_2 (see Fig. 9 and Table S3, ESI†).

It is well noted that major reactions in heterogenous catalysis occur on the surface.[61] In this work, zirconia's surface reactions played a critical role in enabling syngas formation due to the presence of oxygen vacancies (V_O) facilitating the mobility of atomic oxygen.

On the surface the reaction initiates with CO_2 splitting, where CO_2 in the gas phase interacts with a zirconia vacancy, leading to the formation of surface adsorbed CO and O species. In order to confirm this, we compared the signatures of plasma only and the zirconia surface when using pure CO_2 OES, and interestingly we observed the intensities of the atomic oxygen were extremely high in plasma only and drastically reduced with the zirconia packed system, which implies higher adsorption of atomic oxygen on the zirconia surface (see Fig. S9a and b in the ESI†). Based on the measured species of the gas phase *via* OES we hypothesize that firstly, methane underwent dehydrogenation, dissociating into CH radicals and atomic hydrogen. On the zirconia surface, the gas phase exhibited stronger CH* (431 nm) signatures compared to plasma only and looking at the selectivity we can observe higher recombination of methane derived active species in the plasma only system. On the other hand, atomic hydrogen (656.3 nm) levels were lower than in plasma only conditions. This implies a higher recombination of hydrogen in the zirconia-plasma system highlighting the impact of the catalyst-plasma synergistic effect in DMR.

A pathway to mitigate carbon deposition (coking) on zirconia's surface is through the reaction of atomic carbon with atomic oxygen to produce CO in the gas phase. In this scenario, the oxygen migration increases due to the presence of vacancies (V_O) and oxygen species consumed can be replenish. Finally, hydrogen atoms recombine to form molecular hydrogen (H_2 formation). These surface reactions cooperatively improved the syngas generation (see Fig. 10).

3.7. Plausible surface reactions on zirconia

Zirconia's oxygen vacancies (V_O) and mobility of O atoms drive syngas formation (see Fig. 10).

CO_2 splitting:

$$CO_{2(gas)} + V_O \text{ (vacancy in } ZrO_2) \rightarrow CO_{(surf)} + O_{(surf)}$$

CH_4 dehydrogenation:

$$CH_{4(gas)} \rightarrow C_{(surf)} + 4H_{(surf)}$$

Carbon renewal:

$$C_{(surf)} + O_{(surf)} \rightarrow CO_{(gas)} \quad \text{(prevents coking)}$$

H_2 formation:

$$4H_{(surf)} \rightarrow 2H_{2\,(gas)}$$

Table 2 Binding energy (eV) for the pure zirconia (control) *vs.* after plasma exposure

			Binding Energy	Control zirconia	Binding energy	After plasma zirconia
Species	Location		eV	% Area	eV	% Area
O 1s	Zr–O	Lattice oxygen	529.39	43.9	529.11	42.2
	Zr–OH	Surface hydroxyl	530.93	56.0	530.51	42.9
	C–O	Carbon–oxygen	—	—	532.65	14.8
Zr 3d	Zr $3d_{5/2}$	Zr^{4+} sites	181.59	45.7	181.39	50.1
	Zr $3d_{3/2}$	Zr^{4+} sites	183.92	54.2	183.74	49.8

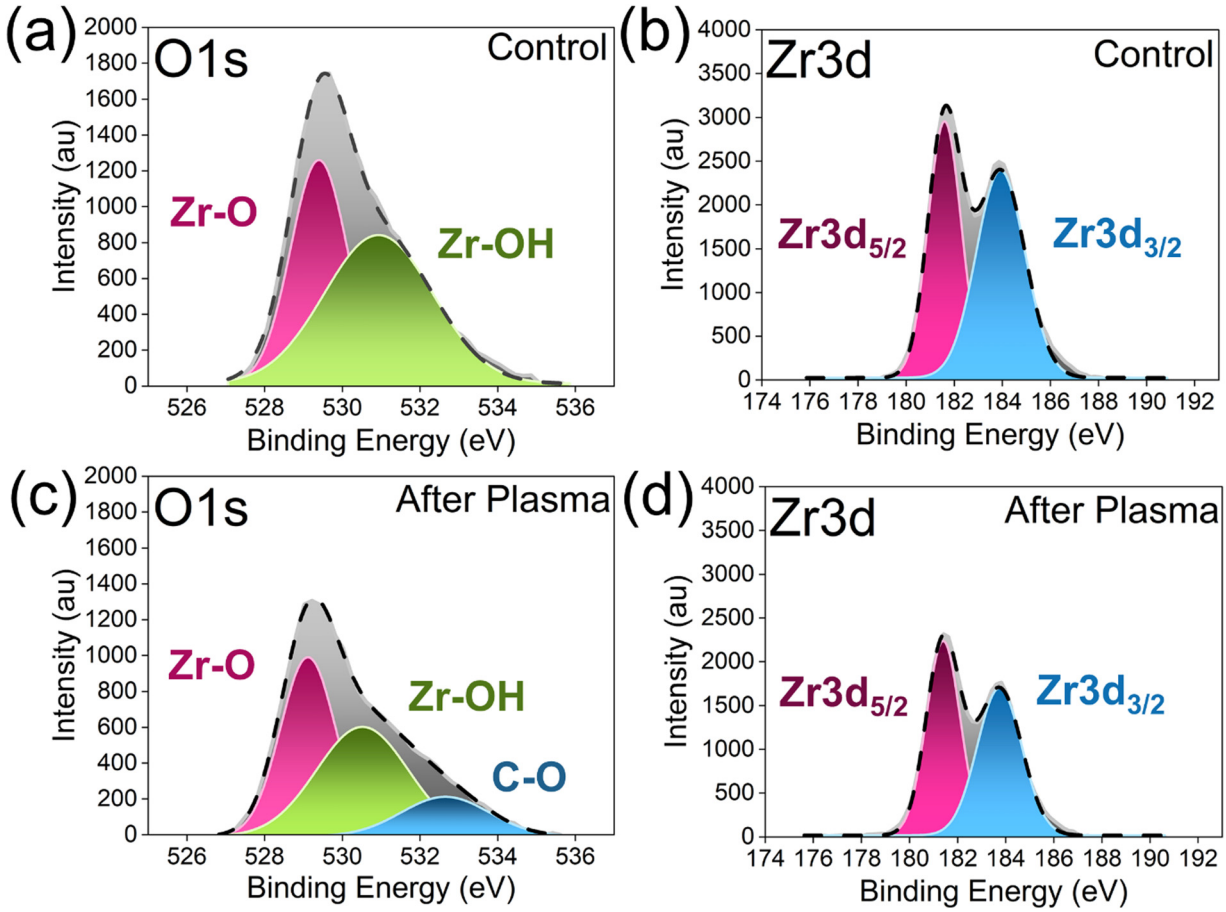

Fig. 8 Comparative X-ray photoelectron spectroscopy (XPS) analysis of zirconia surfaces; panels (a and b) display spectra for pure zirconia (control): (a) O 1s, (b) Zr 3d; panels (c and d) describing to zirconia after plasma exposure: (c) O 1s, (d) Zr 3d.

4. Conclusions

In this study, we explored plasma catalytic dry methane reforming at minimal plasma power (50 watts). This study demonstrated the significant impact of a zirconia-packed bed on plasma-assisted dry reforming of methane (plasma-DRM). Based on the experimental results, introducing zirconia into plasma driven CO_2/CH_4

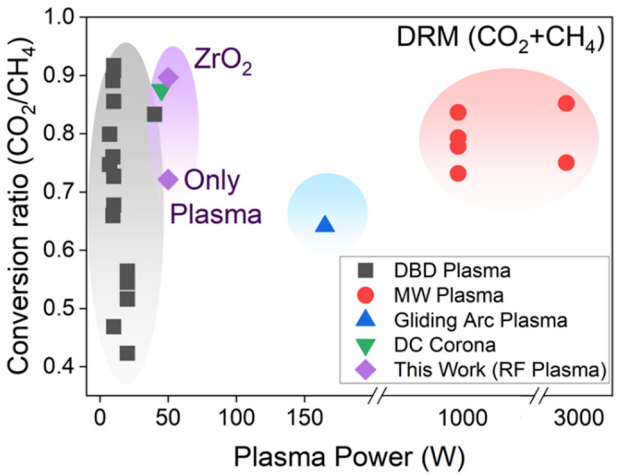

Fig. 9 State of the art plasma-catalytic dry reforming of methane, comparison of (CO_2/CH_4) conversion ratio *vs.* applied plasma power (Watts) for DBD,[12,13,16,69,70] MW,[72,73] GA,[71] DC[77] and this work with RF plasma at low power.

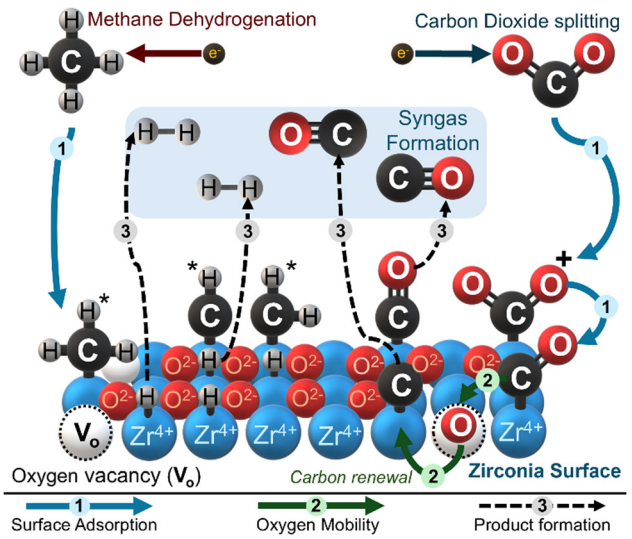

Fig. 10 Plausible plasma catalytic pathway for mitigating coking on the zirconia (ZrO_2) surface.

conversion significantly improves performance. Under plasma-only conditions, CH_4 and CO_2 conversions were 16.5% and 12.0%. Nonetheless, packing the reactor with an inert material such as fumed silica elevated these conversions to 38.4% for CH_4 and 23.4% for CO_2. However, when zirconia (ZrO_2) was packed, the enhancements were even more evident, with methane conversion increased to 63.7% and CO_2 conversion reaching 57.2%. The plasma zirconia synergy facilitated CO_2 decomposition generating CO and oxygen active species increasing syngas (CO and H_2) yields while reducing heavier alkanes and oxygenates. At equimolar feed composition, the CO selectivity rose from 39.5% to 46.5%, and H_2 selectivity increased from 23.7% to 27.5%. The feed composition methane rich 1 : 2 (CO_2 : CH_4) led to lower conversions due to possible methane recombination on the other hand, with CO_2 rich 2 : 1 (CO_2 : CH_4) revealed as the best conversions mitigating the possible methane recombination and leading to higher syngas formation. Optical emission spectroscopy (OES) confirmed that zirconia dramatically increased the CO concentrations in the gas bulk and also favored reactive atomic oxygen species in the gas phase. Stability tests over six hours of plasma operation at 50 W showed no significant changes in zirconia's properties or plasma-catalytic performance, confirming its robustness. In conclusion, zirconia significantly enhanced plasma DRM efficiency, increasing conversion and syngas production while providing understanding of sustainable low temperature plasma DRM systems.

Data availability

Data supporting the findings of this study are available within the article and its ESI.† Additional data can be provided by the authors upon reasonable request.

Conflicts of interest

There are no conflicts to declare.

Acknowledgements

Maria L. Carreon acknowledges NSF-CAREER award No. 2235247.

References

1 D. Pakhare and J. Spivey, *Chem. Soc. Rev.*, 2014, **43**, 7813–7837.
2 C. Palmer, D. C. Upham, S. Smart, M. J. Gordon, H. Metiu and E. W. McFarland, *Nat. Catal.*, 2020, **3**, 83–89.
3 M. L. Carreon, *Nat. Catal.*, 2025, **8**, 2–7.
4 T. Nozaki, D.-Y. Kim and X. Chen, *Jpn. J. Appl. Phys.*, 2024, **63**, 030101.
5 D.-Y. Kim, H. Ham, X. Chen, S. Liu, H. Xu, B. Lu, S. Furukawa, H.-H. Kim, S. Takakusagi and K. Sasaki, *J. Am. Chem. Soc.*, 2022, **144**, 14140–14149.
6 S. Kameshima, K. Tamura, Y. Ishibashi and T. Nozaki, *Catal. Today*, 2015, **256**, 67–75.
7 T. Nozaki, A. Ağıral, S. Yuzawa, J. G. E. H. Gardeniers and K. Okazaki, *Chem. Eng. J.*, 2011, **166**, 288–293.
8 H. M. Nguyen, F. Gorky, S. Guthrie, J. M. Crawford, M. A. Carreon, J. B. Jasinski and M. L. Carreon, *Energy Convers. Manage.*, 2023, **286**, 117082.
9 Y. Ma, X. Han, S. Xu, Z. Li, W. Lu, B. An, D. Lee, S. Chansai, A. M. Sheveleva and Z. Wang, *J. Am. Chem. Soc.*, 2023, **145**, 20792–20800.
10 P. Navascués, J. Cotrino, A. R. González-Elipe and A. Gómez-Ramírez, *Fuel Process. Technol.*, 2023, **248**, 107827.
11 P. Chawdhury, Y. Wang, D. Ray, S. Mathieu, N. Wang, J. Harding, F. Bin, X. Tu and C. Subrahmanyam, *Appl. Catal., B*, 2021, **284**, 119735.
12 Y. Wang, Y. Chen, J. Harding, H. He, A. Bogaerts and X. Tu, *Chem. Eng. J.*, 2022, **450**, 137860.
13 F. Gorky, A. Nambo and M. L. Carreon, *J. CO_2* Util., 2021, **51**, 101642.
14 W. Wang, R. Snoeckx, X. Zhang, M. S. Cha and A. Bogaerts, *J. Phys. Chem. C*, 2018, **122**, 8704–8723.
15 X. Tu and J. C. Whitehead, *Appl. Catal., B*, 2012, **125**, 439–448.
16 L. Wang, Y. Yi, C. Wu, H. Guo and X. Tu, *Angew. Chem.*, 2017, **129**, 13867–13871.
17 D. Mei, X. Zhu, Y.-L. He, J. D. Yan and X. Tu, *Plasma Sources Sci. Technol.*, 2014, **24**, 015011.
18 R. Bellabarba, P. Johnston, S. Moss, C. Sievers, B. Subramaniam, C. Tway, Z. Wang and H. Zhu, *ACS Catal.*, 2023, **13**, 7917–7928.
19 Z. Li, S. Das, P. Hongmanorom, N. Dewangan, M. H. Wai and S. Kawi, *Catal. Sci. Technol.*, 2018, **8**, 2763–2778.
20 J. Newnham, K. Mantri, M. H. Amin, J. Tardio and S. K. Bhargava, *Int. J. Hydrogen Energy*, 2012, **37**, 1454–1464.
21 P. Kumar, Y. Sun and R. O. Idem, *Energy Fuels*, 2007, **21**, 3113–3123.
22 G. D. Yadav and J. J. Nair, *Microporous Mesoporous Mater.*, 1999, **33**, 1–48.
23 D. Liu, X. Y. Quek, W. N. E. Cheo, R. Lau, A. Borgna and Y. Yang, *J. Catal.*, 2009, **266**, 380–390.
24 Ş. Özkara-Aydınoğlu, E. Özensoy and A. E. Aksoylu, *Int. J. Hydrogen Energy*, 2009, **34**, 9711–9722.
25 A. S. A. Al-Fatesh, A. H. Fakeeha and A. E. Abasaeed, *Chin. J. Catal.*, 2011, **32**, 1604–1609.
26 M. Nizio, A. Albarazi, S. Cavadias, J. Amouroux, M. E. Galvez and P. Da Costa, *Int. J. Hydrogen Energy*, 2016, **41**, 11584–11592.
27 R. Snoeckx and A. Bogaerts, *Chem. Soc. Rev.*, 2017, **46**, 5805–5863.
28 H. Puliyalil, D. L. Jurković, V. D. B. C. Dasireddy and B. Likozar, *RSC Adv.*, 2018, **8**, 27481–27508.
29 S. Liu, L. R. Winter and J. G. Chen, *ACS Catal.*, 2020, **10**, 2855–2871.
30 R. Benrabbah, C. Cavaniol, H. Liu, S. Ognier, S. Cavadias, M. E. Gálvez and P. Da Costa, *Catal. Commun.*, 2017, **89**, 73–76.
31 M. Nizio, R. Benrabbah, M. Krzak, R. Debek, M. Motak, S. Cavadias, M. E. Gálvez and P. Da Costa, *Catal. Commun.*, 2016, **83**, 14–17.

32 J. R. Shah, F. Gorky, J. Lucero, M. A. Carreon and M. L. Carreon, *Ind. Eng. Chem. Res.*, 2020, **59**, 5167–5176.
33 J. Shah, F. Gorky, P. Psarras, B. Seong, D. A. Gómez-Gualdrón and M. L. Carreon, *ChemCatChem*, 2020, **12**, 1200–1211.
34 F. Gorky, J. M. Lucero, J. M. Crawford, B. A. Blake, S. R. Guthrie, M. A. Carreon and M. L. Carreon, *Catal. Sci. Technol.*, 2021, **11**, 5109–5118.
35 F. Gorky, A. Best, J. Jasinski, B. J. Allen, A. C. Alba-Rubio and M. L. Carreon, *J. Catal.*, 2021, **393**, 369–380.
36 F. Gorky, J. M. Lucero, J. M. Crawford, B. Blake, M. A. Carreon and M. L. Carreon, *ACS Appl. Mater. Interfaces*, 2021, **13**, 21338–21348.
37 F. Gorky, S. R. Guthrie, C. S. Smoljan, J. M. Crawford, M. A. Carreon and M. L. Carreon, *J. Phys. D: Appl. Phys.*, 2021, **54**, 264003.
38 H. M. Nguyen, F. Gorky, S. Guthrie and M. L. Carreon, *Catal. Today*, 2023, **418**, 114141.
39 F. Gorky, A. Nambo, T. J. Kessler, J. H. Mack and M. L. Carreon, *Ind. Eng. Chem. Res.*, 2023, **62**, 19571–19584.
40 H. M. Nguyen and M. L. Carreon, *ACS Sustainable Chem. Eng.*, 2022, **10**, 9480–9491.
41 J. Shah, J. Lopez-Mercado, M. G. Carreon, A. Lopez-Miranda and M. L. Carreon, *ACS Omega*, 2018, **3**, 455–463.
42 F. Gorky, V. Storr, G. Jones, A. Nambo, J. B. Jasinski and M. L. Carreon, *Membranes*, 2024, **14**, 178.
43 F. Gorky, H. M. Nguyen, K. Krishnan, J. M. Lucero, M. L. Carreon and M. A. Carreon, *ACS Appl. Energy Mater.*, 2023, **6**, 4380–4389.
44 J. Shah, F. Gorky, P. Psarras, B. Seong, D. A. Gómez-Gualdrón and M. L. Carreon, *ChemCatChem*, 2020, **12**, 1200–1211.
45 S. Gershman, H. Fetsch, F. Gorky and M. L. Carreon, *Plasma Chem. Plasma Process.*, 2022, **42**, 731–757.
46 J. R. Shah, J. M. Harrison and M. L. Carreon, *Catalysts*, 2018, **8**, 437.
47 J. Shah, P. Ratnasamy and M. L. Carreon, *Catalysts*, 2017, **7**, 372.
48 F. Gorky, M. A. Carreon and M. L. Carreon, *IOP SciNotes*, 2020, **1**, 024801.
49 J. Shah, T. Wu, J. Lucero, M. A. Carreon and M. L. Carreon, *ACS Sustainable Chem. Eng.*, 2018, **7**, 377–383.
50 F. Gorky, H. M. Nguyen, J. M. Lucero, S. Guthrie, J. M. Crawford, M. A. Carreon and M. L. Carreon, *Chem. Eng. J. Adv.*, 2022, 100340.
51 A. Midilli, H. Kucuk, M. E. Topal, U. Akbulut and I. Dincer, *Int. J. Hydrogen Energy*, 2021, **46**, 25385–25412.
52 A. Vita, G. Cristiano, C. Italiano, L. Pino and S. Specchia, *Appl. Catal., B*, 2015, **162**, 551–563.
53 Y. Zhang, H. Qin, Y. Long, A. Cao, K. Wang, L. Gao, Z. Zhao, H. Zhang, H. Zhang and J. Yan, *Appl. Catal., B*, 2025, **371**, 125206.
54 Y. Long, X. Wang, H. Zhang, K. Wang, W.-L. Ong, A. Bogaerts, K. Li, C. Lu, X. Li and J. Yan, *JACS Au*, 2024, **4**, 2462–2473.
55 P. Aldebert and J. P. Traverse, *J. Am. Ceram. Soc.*, 1985, **68**, 34–40.
56 S. Damyanova, B. Pawelec, K. Arishtirova, M. V. M. Huerta and J. L. G. Fierro, *Appl. Catal., A*, 2008, **337**, 86–96.
57 X. Song, Y. Ding, J. Zhang, C. Jiang, Z. Liu, C. Lin, W. Zheng and Y. Zeng, *J. Mater. Res. Technol.*, 2023, **23**, 648–655.
58 M. O. Zacate, L. Minervini, D. J. Bradfield, R. W. Grimes and K. E. Sickafus, *Solid State Ionics*, 2000, **128**, 243–254.
59 M. Thommes, K. Kaneko, A. V. Neimark, J. P. Olivier, F. Rodriguez-Reinoso, J. Rouquerol and K. S. W. Sing, *Pure Appl. Chem.*, 2015, **87**, 1051–1069.
60 A. Trovarelli, *Catalysis by ceria and related materials*, World Scientific, 2002.
61 I. Langmuir, *Trans. Faraday Soc.*, 1922, **17**, 607–620.
62 E. Devid, D. Zhang, D. Wang, M. Ronda-Lloret, Q. Huang, G. Rothenberg, N. R. Shiju and A. W. Kleyn, *Energy Technol.*, 2020, **8**, 1900886.
63 A. E. Pasto and R. A. Condrate Sr, *J. Am. Ceram. Soc.*, 1973, **56**, 436–438.
64 Y. B. Rajput, A. S. Al-Fatesh, A. I. Osman, M. O. Bayazed, A. A. Ibrahim, A. H. Fakeeha, A. E. Abasaeed, F. S. Almubaddel, O. Alothman and R. Kumar, *Fuel*, 2024, **378**, 132843.
65 A. Bumajdad, A. A. Nazeer, F. Al Sagheer, S. Nahar and M. I. Zaki, *Sci. Rep.*, 2018, **8**, 3695.
66 H. Gu, J. Ding, Q. Zhong, Y. Zeng and F. Song, *Int. J. Hydrogen Energy*, 2019, **44**, 11808–11816.
67 S. R. Teeparthi, E. W. Awin and R. Kumar, *Sci. Rep.*, 2018, **8**, 5541.
68 X. Chen, X. Wang and D. Fang, *Fullerenes, Nanotubes Carbon Nanostruct.*, 2020, **28**, 1048–1058.
69 D. Li, V. Rohani, F. Fabry, A. P. Ramaswamy, M. Sennour and L. Fulcheri, *Appl. Catal., B*, 2020, **261**, 118228.
70 K. Krawczyk, M. Młotek, B. Ulejczyk and K. Schmidt-Szałowski, *Fuel*, 2014, **117**, 608–617.
71 X. Tu and J. C. Whitehead, *Int. J. Hydrogen Energy*, 2014, **39**, 9658–9669.
72 S. Kelly, E. Mercer, R. De Meyer, R.-G. Ciocarlan, S. Bals and A. Bogaerts, *J. CO_2* Util., 2023, **75**, 102564.
73 S. M. Chun, D. H. Shin, S. H. Ma, G. W. Yang and Y. C. Hong, *Catalysts*, 2019, **9**, 292.
74 L. Wang, Y. Yi, C. Wu, H. Guo and X. Tu, *Angew. Chem., Int. Ed.*, 2017, **56**, 13679–13683.
75 D. Li, V. Rohani, F. Fabry, A. P. Ramaswamy, M. Sennour and L. Fulcheri, *Appl. Catal., B*, 2020, **261**, 118228.
76 F. Gorky, V. Storr, J. B. Jasinski and M. L. Carreon, *ACS Mater. Au*, 2025, **5**, 385–396.
77 M.-w Li, G.-h Xu, Y.-l Tian, L. Chen and H.-f Fu, *J. Phys. Chem. A*, 2004, **108**, 1687–1693.